Atomic structure of a rationally engineered gene delivery vector, AAV2.5

Matthew Burg[a], **Claire Rosebrough**[a], **Lauren M. Drouin**[a,1], **Antonette Bennett**[a], **Mario Mietzsch**[a], **Paul Chipman**[a], **Robert McKenna**[a], **Duncan Sousa**[b], **Mark Potter**[c], **Barry Byrne**[c], **R. Jude Samulski**[d], **Mavis Agbandje-McKenna**[a,*]

[a]Department of Biochemistry and Molecular Biology, College of Medicine, McKnight Brain Institute, University of Florida, Gainesville, FL 32610, USA

[b]Biological Science Imaging Resource, Department of Biological Sciences, The Florida State University, 89 Chieftan Way, Rm 119, Tallahassee, FL 32306, USA

[c]Department of Molecular Genetics and Microbiology and Powell Gene Therapy Center, College of Medicine, University of Florida, Gainesville, FL 32610, USA

[d]Department of Pharmacology, Gene Therapy Center, University of North Carolina at Chapel Hill Chapel Hill NC, USA

Abstract

AAV2.5 represents the first structure-guided *in-silico* designed Adeno-associated virus (AAV) gene delivery vector. This engineered vector combined the receptor attachment properties of AAV serotype 2 (AAV2) with the muscle tropic properties of AAV1, and exhibited an antibody escape phenotype because of a modified antigenic epitope. To confirm the design, the structure of the vector was determined to a resolution of 2.78 Å using cryo-electron microscopy and image reconstruction. The structure of the major viral protein (VP), VP3, was ordered from residue 219 to 736, as reported for other AAV structures, and the five AAV2.5 residues exchanged from AAV2 to AAV1, Q263A, T265 (insertion), N706A, V709A, and T717N, were readily interpretable. Significantly, the surface loops containing these residues adopt the AAV1 conformation indicating the importance of amino acid residues in dictating VP structure.

Keywords

Adeno-associated virus; cryo-EM; Vector engineering; Structure-guided design; Parvovirus

1. Introduction

The Adeno-associated viruses (AAVs) are promising gene delivery vectors being developed for therapeutic applications. Current limitations to full realization of this system includes broad tissue tropism and neutralization by pre-existing host antibodies. Strategies to overcome these hurdles are focused on capsid sequence modification utilizing different approaches including error prone PCR, directed evolution, DNA shuffling, and structure-guided surface modifications by site-directed mutagenesis (Drouin and Agbandje-McKenna, 2013). The AAV2.5 chimera, combining features of parental AAV serotype 1 (AAV1) and AAV2, was generated using a structurally guided rational design strategy (Bowles et al., 2012). The vector was engineered with five AAV1 amino acids substituted into AAV2 based on comparison to muscle tropic serotypes AAV1, AAV7, AAV8, and AAV9 (Bowles et al., 2012). AAV2.5 was designed to bind heparan sulfate (HS), similar to AAV2, to display a muscle-tropic phenotype, like AAV1, and to have the ability to evade the immune response against AAV2 (Bowles et al., 2012). These phenotypes have been confirmed (Bowles et al., 2012). The vector was specifically designed to treat Duchenne muscular dystrophy (DMD), a monogenic disease affecting 1 in 5000 male births causing muscle degeneration, loss of mobility, and premature death (Gray et al., 2013; Iyombe-Engembe and Tremblay, 2017; Li et al., 2015; Mendell et al., 2010; Nelson et al., 2017, 2016; Ousterout et al., 2013; Wang et al., 2017). AAV2.5, packaging a miniaturized dystrophin gene, has been evaluated in a Phase I/II clinical trial with 5 pediatric patients and shown a promising safety profile along with gene expression (Bowles et al., 2012).

The AAVs package a single-stranded DNA genome of 4.7 Kb into a non-enveloped T = 1 capsid of ~ 260 Å in diameter. The sixty capsid viral proteins (VPs) assembling the capsids are the overlapping VP1, VP2, and VP3, in a predicted ratio of 1:1:10. The structures of numerous AAV serotypes, including AAV1 and AAV2, have been determined by either X-ray crystallography or cryo-electron microscopy and image reconstruction (cryo-EM), and show that only the VP3 common sequence is ordered. The capsid surface contains determinants of receptor attachment, tissue tropism, and antigenic reactivity, among other functions, within common variable regions (VRs) (Agbandje-McKenna and Kleinschmidt, 2011; Govindasamy et al., 2006; Halder et al., 2012). Here, the structure of AAV2.5 was determined to 2.78 Å using cryo-EM. The structure confirms the use of rational design to achieve desired capsid surface features without loss of the tertiary and quaternary structure to confer functional phenotypes.

2. Materials and methods

2.1. Production and purification

The AAV2.5 CMV GFP vector was produced by triple transfection as previously reported (Bowles et al., 2012). Cell pellets were re-suspended in 20 mM Tris-HCl pH 7.4, 150

mM NaCl and 0.5% OPE (octylphenol ethoxylate, also known as Triton-X 100) as the lysis buffer and processed by a single pass through a microfluidizer then centrifuged at $2560 \times g$ for 10 min to remove cellular debris. This partially clarified lysate was loaded onto a Heparin-6-fast flow column (GE) and washed with 20 mM Tris-HCl pH 7.4, 150 mM NaCl and 0.5% Triton-X 100 buffer followed by 1X PBS. The virus-containing fraction was eluted using 1X PBS with an additional 200 mM NaCl (to ~350 mM NaCl total). The eluted fraction was adjusted to 1 M NaCl (using a 5 M NaCl stock solution). This solution was loaded onto a hydrophobic interaction (Phenyl) column (GE), and the flow through fraction was collected. The 1 M NaCl flow through fraction was diluted to < 100 mM NaCl and subsequently loaded onto an SP Sepharose Fast Flow (SPFF) ion exchange column (GE). The column was washed with 1X PBS and the AAV2.5 vector was eluted with 1X PBS at 350 mM NaCl. The sample purity and integrity was monitored by 10% SDS-PAGE with Coomassie blue staining and electron microscopy (50,000 ×), respectively, and the concentration was determined using UV/visible light (Vis) spectrometry (260/280 nm; molar extinction coefficient, 1.7 for concentration in mg/ml).

2.2. Cryo-EM and data collection

Three microliters of AAV2.5 (~ 1.0 mg/ml) was applied to C-flat holey carbon grids (Protochips, Inc.), following glow discharge to increase hydrophilicity, and vitrified with a Vitrobot Mark IV (FEI Co.). The grids were screened with a Tecnai G2 F20-TWIN transmission electron microscope operated at 200 kV under low-dose conditions (~ 20 $e^-/Å^2$) prior to high resolution data collection. Cryo-EM movie frames were collected on a Titan Krios electron microscope (FEI Co.) operated at 300 kV with a DE20 direct electron detector (Direct Electron). Micrograph frame alignment was performed with the DE_process_frames software with the corresponding dark and bright reference images without radiation dose damage compensation (Spear et al., 2015). The data collection parameters are summarized in Table 1.

2.3. Structure determination by 3D image reconstruction, model building, and structure refinement

The particle image extraction from the aligned micrographs, data pre-processing, and structure determination of the AAV2.5 vector were as previously reported for human bufavirus 2 (Ilyas et al., 2018). The gold standard protocol was followed throughout the structure determination process. The reconstructed map resolution was estimated at FSC = 0.143. Table 1 contains the data collection and refinement parameters. To sharpen the high-resolution features of the map, B-factors 1/50, 1/100, 1/150, and 1/200 $Å^2$, were applied to the map followed by visual inspection in the Coot program (Emsley et al., 2010). The 1/100 map showed the best features for the side- and main-chains and was thus selected for model building in Coot and refinement in the Phenix program (Afonine et al., 2013).

The AAV2.5 cryo-EM map was interpreted using coordinates generated from the AAV2 VP3 sequence with the five residues substitution from AAV1, and with the AAV2 crystal structure (RCSB PDB ID # 1LP3) supplied as a template in the SWISS-MODEL online program (Biasini et al., 2014). The building of a 60-mer model, docking into the cryo-reconstructed map using the "fit in map" subroutine in UCSF-Chimera, and the pixel size

screen to maximize correlation between map and model were conducted as previously described (Ilyas et al., 2018; Mietzsch et al., 2017). The AAV2.5 density map, at 2.78 Å resolution, enabled the interpretation of individual VP3 amino acid positions from N-terminal residue 219–736 (C-terminus) using interactive model building and the real-space-refine option in Coot (Emsley et al., 2010). A 60-mer of the VP3 model was refined against the cryo-reconstructed density map in the Phenix program (Afonine et al., 2013). This involved rigid body, real-space, and B-factor refinement, with the default settings. The model was inspected with Coot between refinement steps, and side- and main-chain modifications were made, when necessary. The final statistics are listed in Table 1. For structural comparison to parental AAV1 and AAV2, the Cα atoms of the VP3 of AAV1, AAV2, and AAV2.5 were superposed using the sequence and secondary structure matching option in the PyMOL program (DeLano, 2002). For figures, side chain density images and cartoon representations were generated with the PyMOL program (DeLano, 2002). Surface representations were generated in the UCSF-Chimera program (Yang et al., 2012).

2.4. Structure accession numbers

The cryo-EM reconstructed density map and atomic model built for the capsid are deposited with accession numbers EMD-7452, PDB ID 6CBE in the Electron Microscopy Data Bank (EMDB).

3. Results and discussion

The purified AAV2.5 vector sample, containing a mixture of full (DNA containing) and empty particles, was used to determine the capsid structure to 2.78 Å resolution from 24,618 individual particle images (Table 1, Fig. 1). Due to the apparent disorder of VP1 and VP2, because of the icosahedral symmetry imposed during structure determination, only residues 219–736, within the VP3 common region, is resolved in the cryo-reconstructed density map (Fig. 1C, Fig. 2A). The VP1u, VP1/2 overlapping region, and the first 14 residues of the VP3 common region, are disordered as has been previously reported for other AAV capsid structures (Halder et al., 2012). As anticipated, the VP3 topology conserves the core eight-stranded antiparallel β-barrel and α-helix A, and the capsid has depressions at the icosahedral 2-fold symmetry axes and surrounding the 5-fold axes, and three separate protrusions surrounding the 3-fold axes, as reported for AAV1 and AAV2 and all other AAVs (Fig. 2A and B) (DiMattia et al., 2012; Govindasamy et al., 2006; Lerch et al., 2010; Nam et al., 2007; Ng et al., 2010; Xie et al., 2002). Loop regions inserted between the core secondary structure elements form the capsid surface and comprise regions, which vary in sequence and structure between the AAVs, termed VRs (Fig. 2A) (Govindasamy et al., 2006).

The wall of the 2-fold depression is formed by α-helix A, VR-VI, and VR-IX; the 3-fold protrusions by VR-IV and VR-VIII from one VP monomer and VR-V from a 3-fold related monomer; and a channel at the 5-fold region is formed by the DE loop (between βD and βE) that form a β-ribbon with VR-II at their apex (Fig. 2). The loop between βH and βI, the HI loop, lines the floor of the depression surrounding the 5-fold channel (Fig. 2). A raised capsid region between the depressions at the 2- and 5-fold axes, referred to as the 2/5-fold

wall, is assembled from VR-I, VR-III, VR-VII, and regions of VR-X. The residue changes engineered into AAV2 to create AAV2.5, Q263A and T265 (insertion) and N706A, V709A and T717N (AAV1 numbers), occur in VR-I and VR-IX, respectively (Figs. 2 and 3). Thus, these residues modify the 2/–5-fold wall as well as the 2-fold region of the capsid (Fig. 3C).

Superposition of the AAV2.5 structure onto AAV1 and AAV2 resulted in root mean square deviation (RMSD) of 0.79 and 0.69 Å, respectively. Significantly, while the majority of the main- and side-chain densities of AAV2.5 is identical to AAV2, the structure of AAV2.5 VR-I follows the loop conformation of AAV1 (Fig. 3A) and the side-chain densities of residues A706, A709, and N717 are consistent with the substituted residue types (Fig. 3E-F). The other AAV2.5 VRs, including the highly divergent VR-IV, follow the conformation of AAV2 (Fig. 3B and D) as evident in the local RMSD values provided in Table 2.

The AAV2.5 vector was designed to acquire the skeletal muscle transduction properties of AAV1 while maintaining the HS binding properties of parental AAV2 and escaping from antibodies targeted at AAV2 (Bowles et al., 2012). The conservation of the VR-I loop conformation between AAV1 and AAV2.5 suggests that the single residue insertion is the structural determinant for VR-I. Importantly, AAV1 residue 265 and other residues within VR-I serve as determinants of tissue tropism and transduction efficiency (Li et al., 2012; Lochrie et al., 2006). Furthermore, residues within VR-I and VR-IX form part of the A20 antibody neutralizing epitope, and the similarity of AAV2.5 to AAV1 at amino acid positions substituted with AAV1 residues confers the antibody escape function on AAV2.5 (Bowles et al., 2012). Finally, while mutations N706A, V709A, and T717N provided AAV2.5 with A20 escape, the main-chain structure of this region is not altered compared to the AAV2 structure and indicates that the residue types determine antibody escape phenotype (Fig. 3).

There are currently several AAV structures available (DiMattia et al., 2012; Govindasamy et al., 2006; Govindasamy et al., 2013; Halder et al., 2015; Lerch et al., 2010; Mikals et al., 2014; Nam et al., 2007; Ng et al., 2010; Xie et al., 2002). The structure of AAV2.5 reported here confirms the structure-guided design strategy, engineered to combine functional features of AAV1 and AAV2. This report shows that future efforts at rational capsid engineering can be guided by information from wild-type AAV capsid structures in addition to functional information on capsid-receptor and capsid-antibody complexes. It also indicates that structure and function can be predicted for chimeric AAV vectors arising from directed evolution and other strategies employed to create novel capsids which combine sequences.

Acknowledgement

References

Afonine PV, Headd JJ, Terwilliger TC, Adams PD 2013. Computational Crystallography Newsletter, pp. 43–44, Vol. 4.

Agbandje-McKenna M, Kleinschmidt J, 2011. AAV capsid structure and cell interactions. Methods Mol. Biol 807, 47–92. [PubMed: 22034026]

Biasini M, Bienert S, Waterhouse A, Arnold K, Studer G, Schmidt T, Kiefer F, Gallo Cassarino T, Bertoni M, Bordoli L, Schwede T, 2014. SWISS-MODEL: modelling protein tertiary and quaternary structure using evolutionary information. Nucl. Acids Res 42, W252–W258. [PubMed: 24782522]

Bowles DE, McPhee SW, Li C, Gray SJ, Samulski JJ, Camp AS, Li J, Wang B, Monahan PE, Rabinowitz JE, Grieger JC, Govindasamy L, Agbandje-McKenna M, Xiao X, Samulski RJ, 2012. Phase 1 gene therapy for Duchenne muscular dystrophy using a translational optimized AAV vector. Mol. Ther 20, 443–455. [PubMed: 22068425]

DeLano WL, 2002. The PyMOL Molecular Graphics System. DeLano Scientific, San Carlos, CA, USA.

DiMattia MA, Nam HJ, Van Vliet K, Mitchell M, Bennett A, Gurda BL, McKenna R, Olson NH, Sinkovits RS, Potter M, Byrne BJ, Aslanidi G, Zolotukhin S, Muzyczka N, Baker TS, Agbandje-McKenna M, 2012. Structural insight into the unique properties of adeno-associated virus serotype 9. J. Virol 86, 6947–6958. [PubMed: 22496238]

Drouin LM, Agbandje-McKenna M, 2013. Adeno-associated virus structural biology as a tool in vector development. Future Virol. 8, 1183–1199. [PubMed: 24533032]

Emsley P, Lohkamp B, Scott WG, Cowtan K, 2010. Features and development of coot. Acta Crystallogr. Sect. D, Biol. Crystallogr 66, 486–501. [PubMed: 20383002]

Govindasamy L, Padron E, McKenna R, Muzyczka N, Kaludov N, Chiorini JA, Agbandje-McKenna M, 2006. Structurally mapping the diverse phenotype of adeno-associated virus serotype 4. J. Virol 80, 11556–11570. [PubMed: 16971437]

Govindasamy L, Dimattia MA, Gurda BL, Halder S, McKenna R, Chiorini JA, Muzyczka N, Zolotukhin S, Agbandje-McKenna M, 2013. Structural insights into adeno-associated virus serotype 5. J. Virol 87, 11187–11199. [PubMed: 23926356]

Gray SJ, Nagabhushan Kalburgi S, McCown TJ, Jude Samulski R, 2013. Global CNS gene delivery and evasion of anti-AAV-neutralizing antibodies by intrathecal AAV administration in non-human primates. Gene Ther. 20, 450–459. [PubMed: 23303281]

Halder S, Ng R, Agbandje-McKenna M, 2012. Parvoviruses: structure and infection. Future Virol. 7, 253–278.

Halder S, Van Vliet K, Smith JK, Duong TT, McKenna R, Wilson JM, Agbandje-McKenna M, 2015. Structure of neurotropic adeno-associated virus AAVrh. 8. J. Struct. Biol 192, 21–36. [PubMed: 26334681]

Ilyas M, Mietzsch M, Kailasan S, Vaisanen E, Luo M, Chipman P, Smith JK, Kurian J, Sousa D, McKenna R, Soderlund-Venermo M, Agbandje-McKenna M, 2018. Atomic resolution structures of human bufaviruses determined by cryo-electron microscopy. Viruses, 10.

Iyombe-Engembe J-P, Tremblay JP, 2017. The advances and challenges of gene therapy for Duchenne muscular dystrophy. J. Genetic Med. Gene Therapy 1, 019–036.

Lerch TF, Xie Q, Chapman MS, 2010. The structure of adeno-associated virus serotype 3B (AAV-3B): insights into receptor binding and immune evasion. Virology 403, 26–36. [PubMed: 20444480]

Li C, Diprimio N, Bowles DE, Hirsch ML, Monahan PE, Asokan A, Rabinowitz J, Agbandje-McKenna M, Samulski RJ, 2012. Single amino acid modification of adeno-associated virus capsid changes transduction and humoral immune profiles. J. Virol 86, 7752–7759. [PubMed: 22593151]

Li HL, Fujimoto N, Sasakawa N, Shirai S, Ohkame T, Sakuma T, Tanaka M, Amano N, Watanabe A, Sakurai H, Yamamoto T, Yamanaka S, Hotta A, 2015. Precise correction of the dystrophin gene in duchenne muscular dystrophy patient induced pluripotent stem cells by TALEN and CRISPR-Cas9. Stem Cell Rep. 4, 143–154.

Lochrie MA, Tatsuno GP, Christie B, McDonnell JW, Zhou S, Surosky R, Pierce GF, Colosi P, 2006. Mutations on the external surfaces of adeno-associated virus type 2 capsids that affect transduction and neutralization. J. Virol 80, 821–834. [PubMed: 16378984]

Mendell JR, Campbell K, Rodino-Klapac L, Sahenk Z, Shilling C, Lewis S, Bowles D, Gray S, Li C, Galloway G, Malik V, Coley B, Clark KR, Li J, Xiao X, Samulski J, McPhee SW, Samulski RJ, Walker CM, 2010. Dystrophin immunity in Duchenne's muscular dystrophy. N. Engl. J. Med 363, 1429–1437. [PubMed: 20925545]

Mietzsch M, Kailasan S, Garrison J, Ilyas M, Chipman P, Kantola K, Janssen ME, Spear J, Sousa D, McKenna R, Brown K, Soderlund-Venermo M, Baker T, Agbandje-McKenna M, 2017. Structural insights into human bocaparvoviruses. J. Virol 91.

Mikals K, Nam HJ, Van Vliet K, Vandenberghe LH, Mays LE, McKenna R, Wilson JM, Agbandje-McKenna M, 2014. The structure of AAVrh32.33, a novel gene delivery vector. J. Struct. Biol 186, 308–317. [PubMed: 24704217]

Nam HJ, Lane MD, Padron E, Gurda B, McKenna R, Kohlbrenner E, Aslanidi G, Byrne B, Muzyczka N, Zolotukhin S, Agbandje-McKenna M, 2007. Structure of adeno-associated virus serotype 8, a gene therapy vector. J. Virol 81, 12260–12271. [PubMed: 17728238]

Nelson CE, Robinson-Hamm JN, Gersbach CA, 2017. Genome engineering: a new approach to gene therapy for neuromuscular disorders. Nature reviews. Neurology 13, 647–661. [PubMed: 28960187]

Nelson CE, Hakim CH, Ousterout DG, Thakore PI, Moreb EA, Castellanos Rivera RM, Madhavan S, Pan X, Ran FA, Yan WX, Asokan A, Zhang F, Duan D, Gersbach CA, 2016. In vivo genome editing improves muscle function in a mouse model of Duchenne muscular dystrophy. Science 351, 403–407. [PubMed: 26721684]

Ng R, Govindasamy L, Gurda BL, McKenna R, Kozyreva OG, Samulski RJ, Parent KN, Baker TS, Agbandje-McKenna M, 2010. Structural characterization of the dual glycan binding adeno-associated virus serotype 6. J. Virol 84, 12945–12957. [PubMed: 20861247]

Ousterout DG, Perez-Pinera P, Thakore PI, Kabadi AM, Brown MT, Qin X, Fedrigo O, Mouly V, Tremblay JP, Gersbach CA, 2013. Reading frame correction by targeted genome editing restores dystrophin expression in cells from Duchenne muscular dystrophy patients. Mol. Ther 21, 1718–1726. [PubMed: 23732986]

Spear JM, Noble AJ, Xie Q, Sousa DR, Chapman MS, Stagg SM, 2015. The influence of frame alignment with dose compensation on the quality of single particle reconstructions. J. Struct. Biol 192, 196–203. [PubMed: 26391007]

Wang JZ, Wu P, Shi ZM, Xu YL, Liu ZJ, 2017. The AAV-mediated and RNA-guided CRISPR/Cas9 system for gene therapy of DMD and BMD. Brain Dev. 39, 547–556. [PubMed: 28390761]

Xie Q, Bu W, Bhatia S, Hare J, Somasundaram T, Azzi A, Chapman MS, 2002. The atomic structure of adeno-associated virus (AAV-2), a vector for human gene therapy. Proc. Natl. Acad. Sci. U.S.A 99, 10405–10410. [PubMed: 12136130]

Yang Z, Lasker K, Schneidman-Duhovny D, Webb B, Huang CC, Pettersen EF, Goddard TD, Meng EC, Sali A, Ferrin TE, 2012. UCSF Chimera, MODELLER, and IMP: an integrated modeling system. J. Struct. Biol 179, 269–278. [PubMed: 21963794]
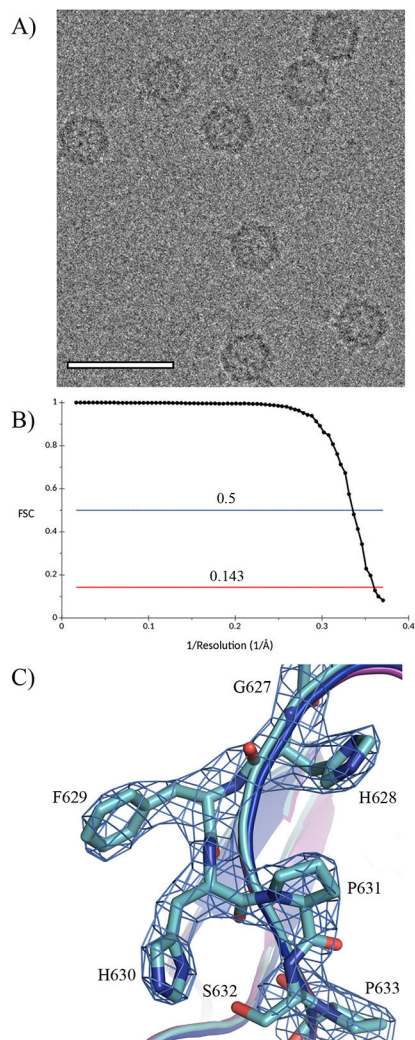
Fig. 1.
Structure determination of AAV2.5. A) Cryo-electron micrograph of AAV2.5. Scale bar is 500 Å. B) Fourier Shell Correlation (FSC) plot from the last cycle of structure refinement. FSC 0.5 and FSC 0.143 are indicated. C) Piece of AAV2.5 electron density (blue mesh) showing residues 627–6333 to exemplify the quality of the map at 2.78 Å resolution. Residue types and number are as labeled. The main chain is also shown for AAV1 (purple), AAV2 (blue), and AAV2.5 (niobium).
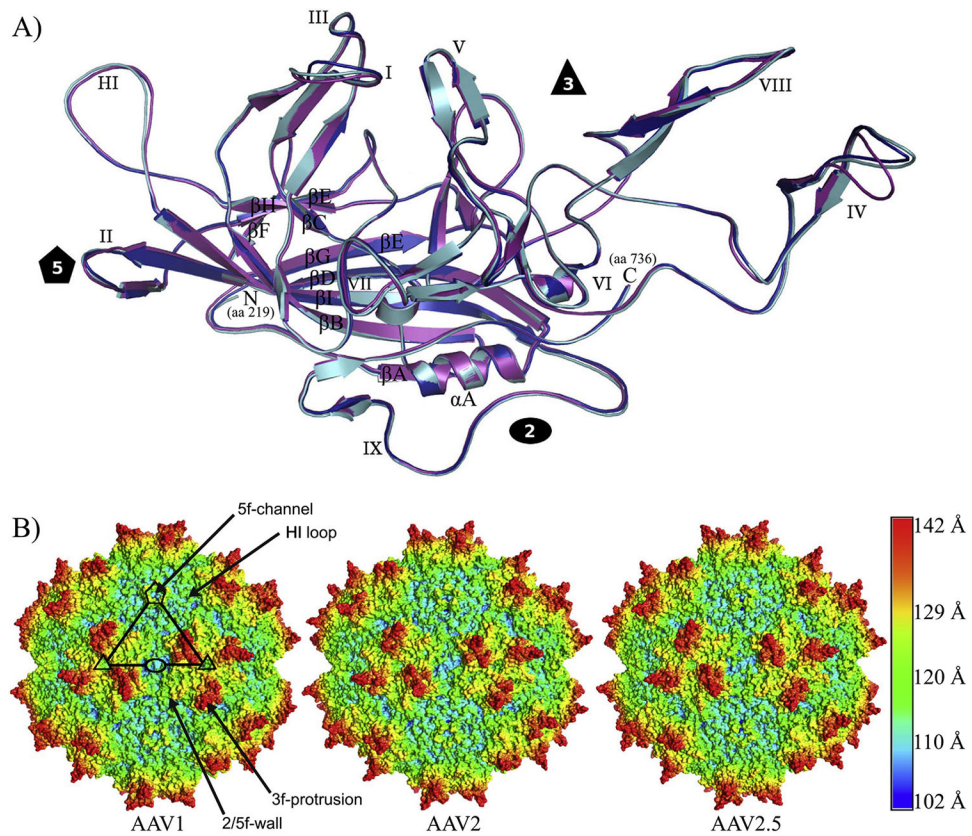
Fig. 2.
Comparison of the AAV2.5 structure to AAV1 and AAV2. A) Superposition of the AAV1 (purple), AAV2 (blue), and AAV2.5 (niobium) VP3 structures. The position of the VRs within VP3 are indicated. The N- and C-term, and HI loop are labeled. The β-strands and α-A helix are labeled. The approximate 2-, 3-, and 5-fold axes are indicated with an oval, triangle, and pentagon, respectively. The two VRs with significant conformational differences are VR-I and VR-IV. B) Capsid surface maps generated from 60mer coordinates of AAV1, AAV2, and AAV2.5. These are radially colored from blue to red based on distance from the particle center in Å as indicated in the scale bar. The viral asymmetric unit is shown above the AAV1 capsid with 2-, 3-, and 5-fold axes connected by a triangle and indicated as in A). The 2-/5-fold wall is the same in AAV1 and AAV2.5 while the 3-fold protrusions are the same in AAV2 and AAV2.5 due to the conformations of VR-I and VR-IV, respectively.
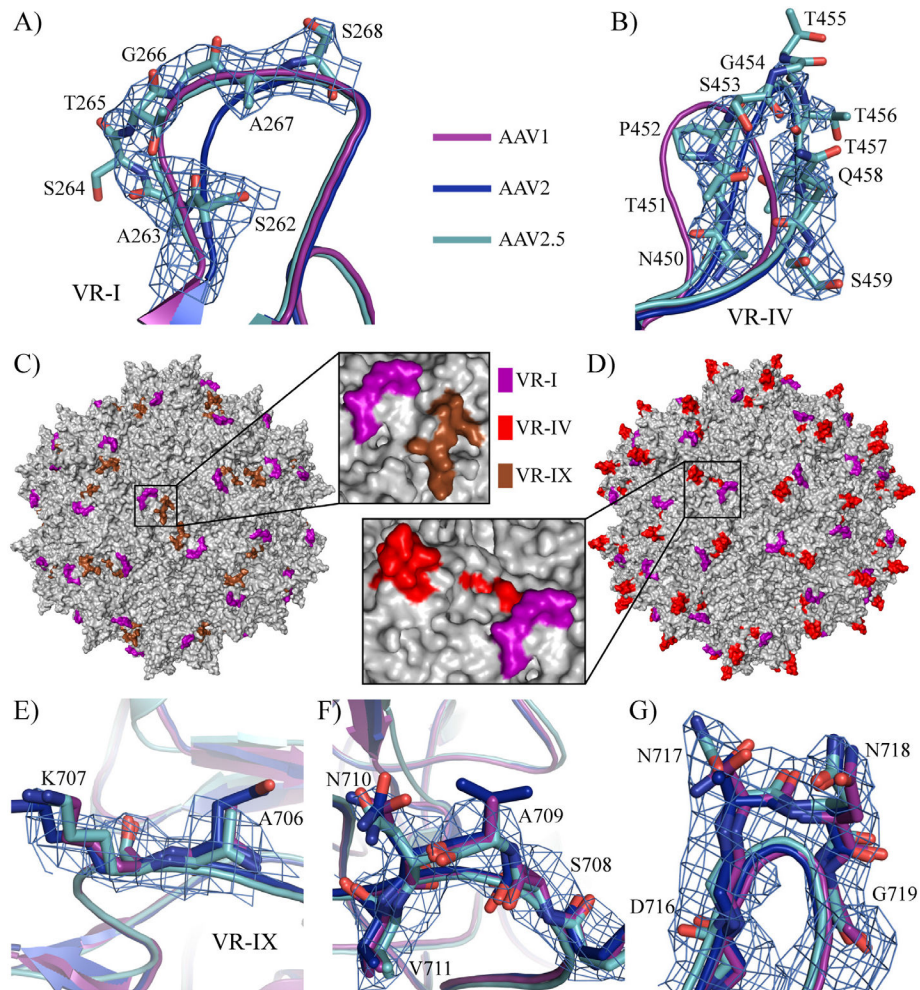
Fig. 3.
Structural differences in AAV2.5. A) Density for AAV2.5 VR-I and B) VR-IV. The AAV1, AAV2.5, and AAV2 main chain are shown in purple, niobium, and blue, respectively. The AAV2.5 residue types and numbers are as labeled. The VR-IV density in (B) is shown to demonstrate that unmodified surface loops in AAV2.5 adopt the AAV2 conformation. C and D) Capsid surface maps for 60mer coordinates of AAV2.5 in grey with VR-I and VR-IX highlighted in purple and brown and VR-I and VR-IV in purple and red, respectively. The proximity of these regions on the capsid surface is evident in these images as shown in the zoomed in views to the right and left, respectively, in C and D, of the capsid surface maps. E, F, and G) Density (blue mesh) for point mutations N706A, V709A, and T717N (AAV2.5 numbering), respectively. These are consistent with the amino acid substitutions. The residue numbers and type are as labeled. The main chain for AAV1, AAV2.5, and AAV2 are as indicated in panels A and B.

Table 1

Data collection parameters and statistics of final model.

Total number of micrographs	1592
Defocus range (μm)	0.6–4.0
Electron dose ($e^-/\text{Å}^2$)	59.34
No. of frames/micrograph	35
Pixel size (Å/pixel)	0.95
Starting no. of particles	30,773
No. of particles used for final map	24,618
Inverse B factor used for final map (Å^2)	1/100
Resolution of final map (Å)	2.78
PHENIX model refinement statistics	
Residue range	219–736
Map CC	0.871
RMSD (Å)	
Bonds	0.01
Angles	0.79
All-atom clash score	7.56
Ramachandran plot (%)	
Favored	98.26
Allowed	1.74
Outliers	0
Rotamers outliers	0
No. of Cβ deviations	0

Table 2

Overall RMSD (in Å) for the aligned AAVs and local RMSD (in Å) in the VRs (bold indicates large divergence).

	Overall RMSD	VR-I	VR-II	VR-III	VR-IV	VR-V	VR-VI	VR-VII	VR-VIII	HI-loop	VR-IX
AAV1 vs. AAV2.5	0.79	0.62	2.11	0.71	2.70	0.79	0.67	0.96	0.74	0.72	0.38
AAV2 vs. AAV2.5	0.69	2.86	1.67	0.51	1.29	0.67	0.71	0.47	0.62	0.60	0.49
AAV1 vs. AAV2	0.85	3.00	0.88	0.66	2.83	0.92	0.37	1.02	0.61	0.43	0.44